



A pragmatic approach for the evaluation of depth-sensing indentation in the self-similar regime

Mahdavi, Hamidreza; Poullos, Konstantinos; Niordson, Christian F.

Published in:
Journal of Applied Mechanics

Link to article, DOI:
[10.1115/1.4052218](https://doi.org/10.1115/1.4052218)

Publication date:
2022

Document Version
Peer reviewed version

[Link back to DTU Orbit](#)

Citation (APA):
Mahdavi, H., Poullos, K., & Niordson, C. F. (2022). A pragmatic approach for the evaluation of depth-sensing indentation in the self-similar regime. *Journal of Applied Mechanics*, 89(1), Article 011004 .
<https://doi.org/10.1115/1.4052218>

General rights

Copyright and moral rights for the publications made accessible in the public portal are retained by the authors and/or other copyright owners and it is a condition of accessing publications that users recognise and abide by the legal requirements associated with these rights.

- Users may download and print one copy of any publication from the public portal for the purpose of private study or research.
- You may not further distribute the material or use it for any profit-making activity or commercial gain
- You may freely distribute the URL identifying the publication in the public portal

If you believe that this document breaches copyright please contact us providing details, and we will remove access to the work immediately and investigate your claim.

A pragmatic approach for the evaluation of depth-sensing indentation in the self-similar regime

Hamidreza Mahdavi^{a,*}, Konstantinos Poullos^a, Christian F. Niordson^a

^a*Department of Mechanical Engineering, Section of Solid Mechanics, Technical University of Denmark, Nils Koppels Allé, Building 404, DK-2800 Kgs. Lyngby*

Abstract

This work evaluates and revisits elements from the depth-sensing indentation literature by means of carefully chosen practical indentation cases, simulated numerically and compared to experiments. The aim is not to provide a comprehensive study, but to close a series of debated subjects, which constitute major sources of inaccuracies in the evaluation of depth-sensing indentation data in practice, with the help of illustrative examples. Firstly, own examples and references from the literature are presented in order to demonstrate how crucial self-similarity detection and blunting distance compensation are, for establishing a rigorous link between experiments and simple sharp-indenter models. Moreover, it is demonstrated, once again, in terms of clear and practical examples, that no more than two parameters are necessary to achieve an excellent match between a sharp indenter finite element simulation and experimental force-displacement data. The clear conclusion is that reverse analysis methods promising to deliver a set of three unique material parameters from depth-sensing indentation cannot be reliable. Lastly, in light of the broad availability of modern finite element software, we also suggest to avoid the rigid indenter approximation, as it is shown to lead to unnecessary inaccuracies. All conclusions from the critical literature review performed lead to a new semi-analytical reverse analysis method, based on available dimensionless functions from the literature and a calibration against case specific finite element simulations. Implementations of the finite element model employed are released as supplementary material, for two major finite element software packages.

Keywords: Self-similar indentation, Indenter bluntness, Indenter compliance, Finite element analysis, Reverse analysis

1. Introduction

Depth-sensing indentation represents one of the most widely used methods for obtaining mechanical properties of structural materials at the micron and nano-scales [1]. For this reason, the evaluation of indentation experiments has in the past decades been subject

*Corresponding author: hamah@mek.dtu.dk

of very extensive research. Most of the proposed methods build upon the seminal work by Oliver and Pharr [2, 3] which comprises an early comprehensive analysis of load-displacement data from indentation tests. Another central work in the area is the one by Dao et al. [4], who have combined a dimensional analysis of the indentation process and a parametric finite element study into a semi-analytical forward and reverse analysis method. Many other research works based on the same idea can be found in the literature [5–14]. All these methods rely on a perfectly sharp indenter model, for which the loading part of the force-displacement curve, during an indentation test, follows Kick’s law

$$P = Ch^2 \tag{1}$$

where P is the normal force, h is some linear measure of penetration, and C is a constant.

Unlike the many ad-hoc phenomenological relationships involved in different indentation evaluation methods, Kick’s law has a rigorous geometrical and mechanical foundation. Any self-similar conical or pyramidal indentation process will follow Kick’s law exactly, while for planar wedge indentation, the corresponding relationship with the exponent equal to one applies. Hence, Kick’s law is only subject to the well defined self-similarity requirements:

- R1. Substrate and indenter materials are homogeneous and free of size-effects (e.g. strain-gradient effects).
- R2. The form of the indenter is self-similar, i.e. its cross section grows with the square of the distance from the sharp indenter tip. Axisymmetry is not required.
- R3. Absence of adhesion forces.

Under these conditions, any deviation from Kick’s law should be attributed to measurement or evaluation errors. Otherwise, a physical source of violation of self-similarity must be determined by a more thorough investigation of the indenter geometry (cf. R1), the substrate material (cf. R2), [15–17], and possible remote interactions (cf. R3).

Despite the universality of Kick’s law, its correct application implies a proper definition of the penetration measure h . In principle, any length involved in the geometry of a self-similar indent can be used as a penetration measure in Eq. (1) provided that it vanishes just when the very tip of the infinitely sharp indenter comes into contact with the substrate surface. For example, the original work by Oliver and Pharr [2] considers the contact height h_c as the penetration measure used in Eq. (1). Adopting different penetration measures leads to scaled variants of the constant C , but apart from that, there are no essential consequences from adopting any specific penetration measure as long as the chosen length develops self-similarly with the deformation field during indentation.

This requirement on the penetration measure h is of utter importance when Kick’s law is to be applied to not perfectly sharp indenters, as is the case in all real experiments. Figure 1 illustrates this by means of numerical simulations for one sharp and two slightly blunted conical indenters. If a penetration measure \check{h} is defined, with regard to the positioning of the indenters shown in Figure 1a, without correcting for the blunting distance, severe deviations are observed in terms of the obtained force-displacement curves. If, on the contrary, the penetration measure h is defined properly, including the necessary blunt-

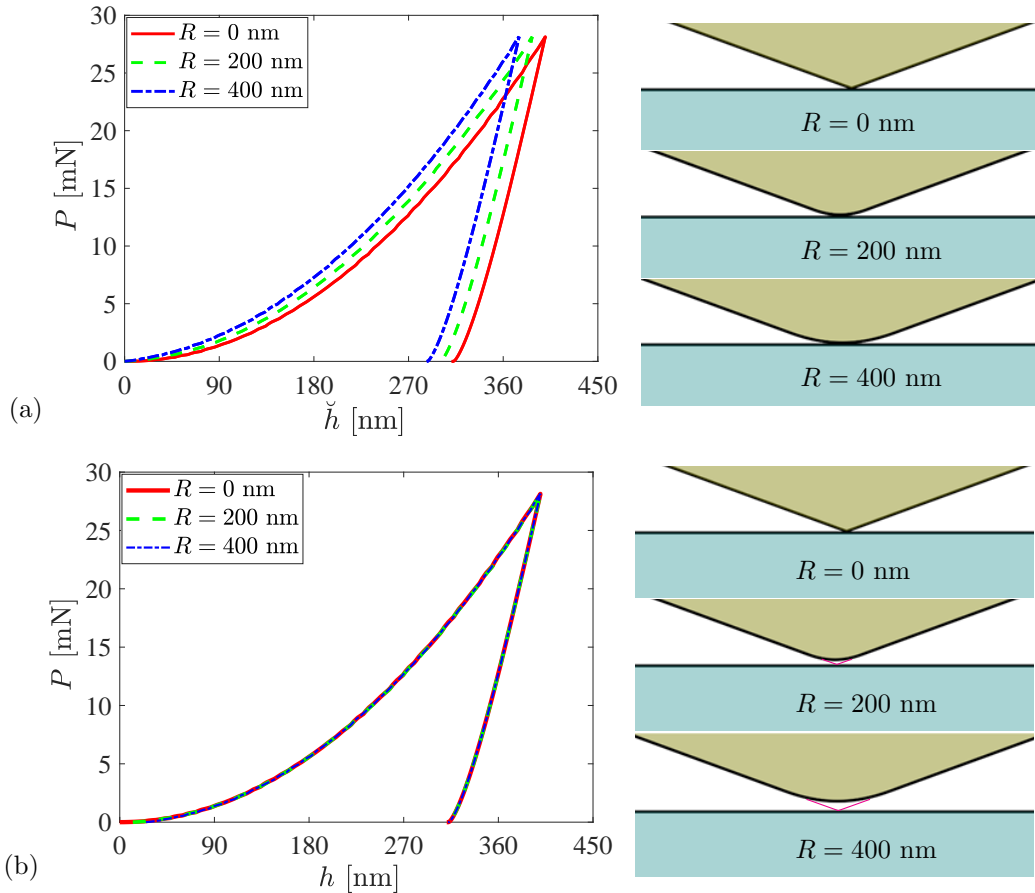


Figure 1: Simulated conical indentation curves illustrating the importance of a correct definition of the penetration distance for the application of Kick’s law with slightly blunted indenters: a) without and b) with blunting distance compensation. The indenter material is diamond and the substrate corresponds to high strength steel.

ing distance compensation shown in Figure 1b, the obtained force-displacement curves are practically independent of the blunting radius and fulfil Kick’s law very precisely.

The importance of proper blunting distance compensation, illustrated in Figure 1, is well understood and described in the literature [18–25]. Nevertheless, it is too often overseen, leading to unfortunate attempts to interpret experimental curves, equivalent to the ones of Figure 1a, by revisiting Kick’s law by ad-hoc modifications of its exponent or by use of different polynomials. Such cases were discussed and rectified, for example, in [23, 26].

Another important aspect in the evaluation of indentation experiments is the deformability of the indenter. All popular semi-analytical approaches assume that the elasticity of the indenter can be accounted for by considering a rigid indenter against an equivalent substrate with accordingly adapted elasticity properties [27]. However, more in-depth investigations have shown that this reduced elastic modulus approximation may lead to significant deviations [22, 28]. Moreover, it introduces ambiguities that may lead to significant mistakes when applied to methods that are based on elasto-plastic finite element parametric studies with a rigid indenter.

The present work also reviews and discusses the current understanding regarding the non-uniqueness of a three-parameter material description for the substrate, with respect to load-displacement curves from a single indenter. Chen et al. [29] have clearly demonstrated that for most structural materials, it is not possible to extract both yield limit and hardening behavior from a single indentation load-displacement curve. Nevertheless, older reverse analysis methods [4], which claim a unique solution for the modulus of elasticity, plastic yield limit, and hardening exponent, are still widely in use. Neglecting the clear findings by Chen et al. [29] and others [6, 10, 30, 31], new methods are still being proposed based on the unrealistic expectation that three substrate material parameters can be extracted from a single indentation load-displacement curve [12, 32]. Unfortunately, unrealistic expectations in this regard can in fact lead to unreliable results, especially when such reverse analysis algorithms are applied in a black box manner. For this reason, the present work brings the uniqueness aspect to the reader's attention by an illustrative example and a discussion of the relevant literature.

Moreover, semi-analytical methods fitted to parametric finite element studies are typically limited to a Poisson's ratio of 0.3. They are also limited to the conical approximation of the real pyramidal geometry. On the contrary, direct use of finite element modeling, as proposed e.g. by Kang et al. [32], allows to use the exact Poisson's ratio even for less common substrate materials and is easily extensible to the real pyramidal indenter geometry.

By means of specific, practical, and illustrative examples and a critical review of the literature, the present work demonstrates how direct modeling is more accurate, less ambiguous, less prone to mistakes, and actually simpler than semi-analytical methods. A hybrid approach is also proposed for calibrating a new semi-analytical reverse analysis method against direct simulations on a per case basis, as a means of avoiding unnecessary inaccuracies. Moreover, to avoid duplication of modeling effort in the future, the present work releases parametric models for conical indentation between an elastic indenter and an elasto-plastic substrate, implemented in ABAQUS and ANSYS Workbench, as supplementary material.

In total, based on a critical selection from the available literature, a systematic, holistic, and pragmatic method is proposed, comprising of a series of essential components

- detection of self-similarity in indentation experiments and cancellation of tip bluntness effects in experimental data (Section 2 and [25]),
- realistic expectations regarding the uniqueness of a reverse analysis with regard to the hardening exponent (Section 3 and [29, 30]),
- publicly released parametric finite element models for indentation (cf. Section 3),
- quantitative understanding of the equivalent rigid indenter approximation as a source of inaccuracy in semi-analytical models (Section 4), and
- a simple reverse analysis method for substrate stiffness and yield limit, including a re-calibration procedure against finite element simulations (Section 5).

2. Self-similarity detection and blunting distance compensation

As explained in the introduction, Kick’s law, expressed by Eq. (1), is an inherent, undisputable characteristic of self-similar indentation processes. For this reason, assessing systematically if a given measurement is classified as self-similar or not is an absolutely essential first step when evaluating an indentation load-displacement curve. Depending on the outcome of this verification step, either the simple methods can be used that the present work and most of the available literature deals with or more specialized evaluation procedures and additional measurements will be necessary [33–35].

This section describes how to practically identify, with a high level of confidence, whether a given indentation measurement lies within the self-similar regime. This will allow to exploit Kick’s law in order to enhance the quality of the experimental data and use a simpler and more accurate procedure for extracting substrate material parameters. Identification of self-similarity in indentation experiments is already discussed in [36] where four possible presentation formats were proposed for force-displacement data. Figure 2 presents the respective data from Figure 1a in two of these formats and demonstrates that plotting the square root of the measured force as a function of the indenter penetration, as in Figure 2a, is the ideal format for evaluating self-similarity. In Figure 2a, not only the loading part of each curve appears very linear almost in its entire extent, but the form and slope of the obtained curves are independent of the tip blunting, except for a horizontal offset, which can easily be corrected as shown in [25].

In reality, there is no perfectly sharp indenter, and simply plotting the recorded force P as a function of a recorded indentation displacement \check{h} will lead to some arbitrary curve within a range of curves like those shown in Figure 1a. Fortunately, as Figure 1b illustrates, the essential information contained in each measurement is independent of the tip blunting. Experimental results can be easily converted to their ideal indenter equivalent, simply by converting the measured indentation displacement \check{h} to its sharp indenter equivalent

$$h = \check{h} + \Delta h, \quad (2)$$

where Δh is the blunting distance defined schematically in Figure 3.

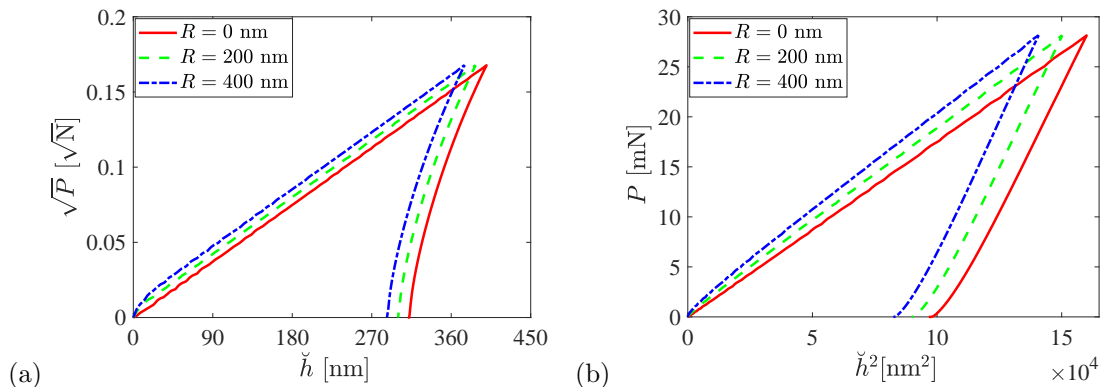


Figure 2: Possible presentations formats for indentation force-displacement data, with regard to identification of self-similarity.

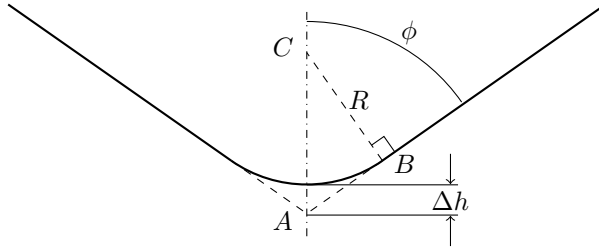


Figure 3: Schematic of the blunted conical indenter, with the definition of the blunting distance Δh .

This correction, identified very early by Murakami et al. [18] and used since by many others [22, 25, 37], is crucial for relating any experimental measurement to numerical, semi-analytical, or analytical methods developed on the basis of a perfectly sharp indenter. When applied to Kick’s law for example, it results in the relationship

$$\sqrt{P} = \sqrt{C}(\check{h} + \Delta h), \quad (3)$$

which provides the basis for assessing self-similarity in experimental \sqrt{P} - \check{h} curves, similar to the ones of Figure 2a. At the same time, it forms the basis for estimating Δh .

The procedure is demonstrated in Figure 4 by means of two real indentation examples. The first example corresponds to Berkovich indentation of a high strength steel sample. In most of its extent, the plotted \sqrt{P} - \check{h} curve follows the linear relationship according to Eq. (3). A linear regression in the portion of the experimental data for $P > 0.1P_{\max}$ furnishes the two constants C and Δh for this measurement, reported in Figure 4a. In Figure 4b, the same procedure is applied to a case of Berkovich indentation on fused silica by Bruns et al. [38]. For both cases, the effect of the calculated blunting distance corrections of respectively 29.4 nm and 18.7 nm on the obtained force-displacement curves is illustrated in the corresponding graphs on the right hand side of Figure 4.

Although the blunting distance Δh can also be calculated geometrically, if the exact indenter tip geometry is known, it is still preferable to estimate Δh directly by fitting Eq. (3) to a measurement. In this manner, the estimated blunting distance correction Δh will also account for other sources of discrepancies, such as surface roughness and deviations in the initial contact detection. In total, the linear fitting of Eq. (3) to an experimental \sqrt{P} - \check{h} curve allows to verify if an indentation is indeed in the self-similar regime and provides a blunting distance correction Δh without relying on prior knowledge or calibration of the indenter form.

Applying the blunting distance correction upfront as a post-processing of the experimental data, rather than as a numerical correction later in the evaluation procedure, is a strongly recommendable practice due to several advantages. Reporting the shifted curves, shown for example on the right hand side of Figure 4, makes published data from different laboratories directly comparable to each other. At the same time, the experimental force-displacement curves after blunting distance compensation are made directly comparable to numerical simulation performed with a perfectly sharp indenter geometry. This circumvents the requirement of including the exact tip rounding in a finite element model which unnecessarily adds complexity and reduces the generality of the model.

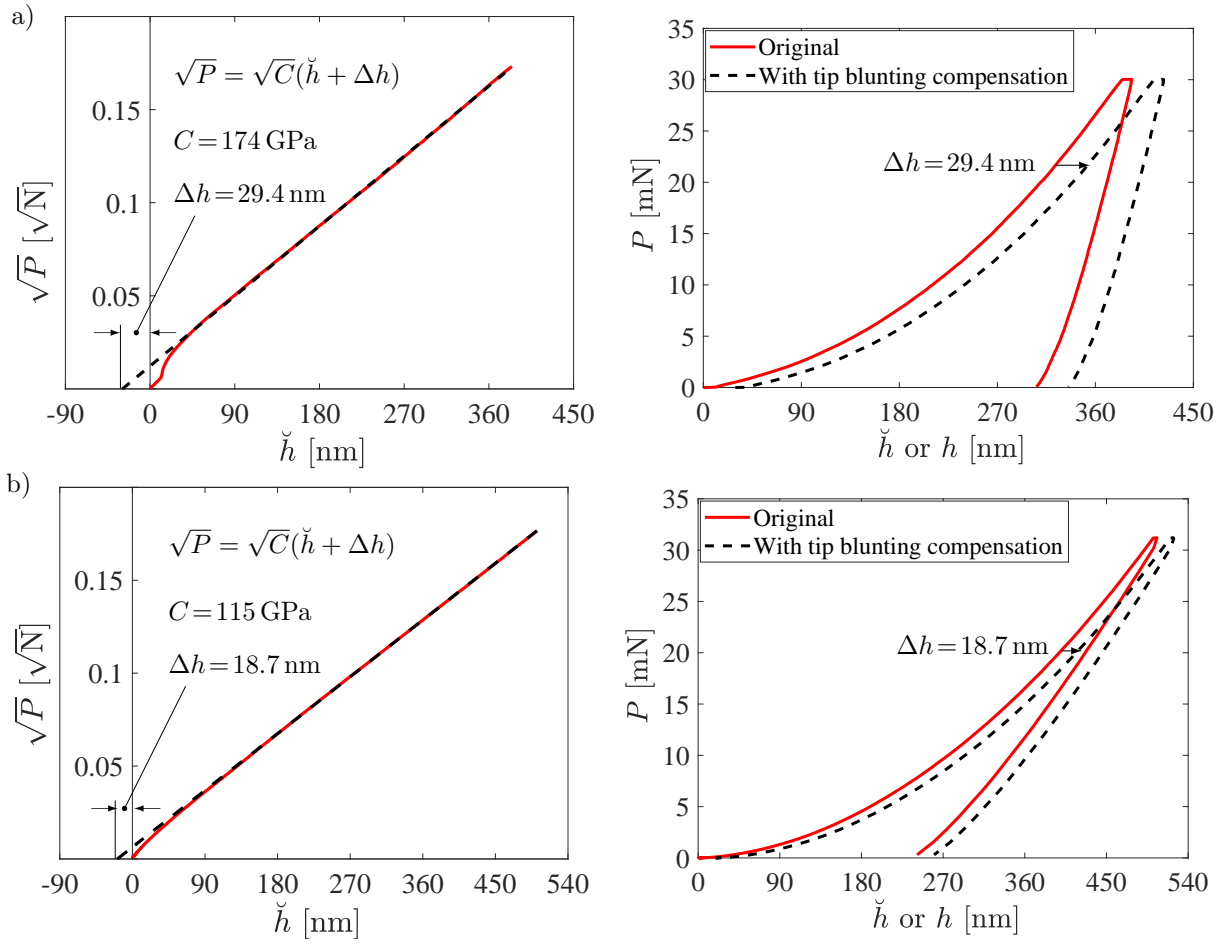


Figure 4: Blunting distance estimation and compensation for indentation measurements on hardened steel (a), and fused silica from [38], (b).

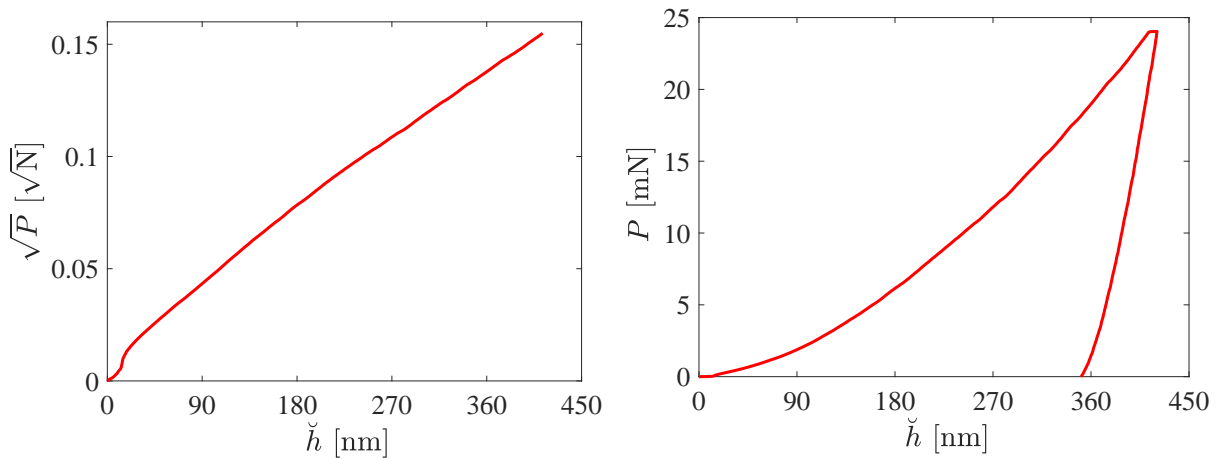


Figure 5: Example of non self-similar indentation experiment on a different type of hardened steel.

When evaluating indentation experiments at sub-micron indentation depths, size-effects may lead to a response which is not self-similar. Although, self-similarity is verified in the measurements shown in Figure 4, it is not uncommon at such small indentation depths that size-dependence exists. For example, the indentation measurement shown in Figure 5, is not self-similar. In many cases, strain gradient plasticity effects, or other violations among the three self-similarity conditions, mentioned in the introduction, will manifest themselves as deviations from linearity in a $\sqrt{P}-\dot{h}$ plot. Comparing the $\sqrt{P}-\dot{h}$ plots between Figures 4 and 5, the difference between a self-similar and a non self-similar indentation curve becomes apparent. Such a clear conclusion cannot readily be drawn from $P-\dot{h}$ plots, which are normally used in the depth-sensing indentation literature. The aim of the present work is not to address the cases that exhibit size effects, but to underline the importance of systematically verifying self-similarity, before applying any reverse analysis method from the literature that relies on self-similarity.

3. Finite element model based evaluation of depth-sensing indentation

A sharp indenter model can quite precisely represent experiments performed with a blunted indenter as long as blunting distance compensation is applied to the experimental data. This observation significantly simplifies the application of finite element modeling to the evaluation of indentation experiments. Moreover, commercial general purpose finite element software is today much more accessible, powerful, and easy to use compared to the time of early finite element analyses of indentation [4]. Direct finite element modeling of self-similar indentation is actually now less complex and less error-prone than the use of semi-analytical approximations fitted to parametric studies [4, 12]. It is not to underestimate that the direct modeling approach also circumvents a series of important sources of inaccuracies and restrictions of the semi-analytical methods, discussed in the subsequent sections. This section presents a standard finite element model for self-similar indentation, released as supplementary material in Appendix D, and demonstrates its usage for a manual reverse analysis of the experimental load-displacement curves from the previous section.

Figure 6 shows the finite element mesh of the axisymmetric two-dimensional model for an elastic conical indenter with a half-included angle of 70.3° , pressed into an elasto-plastic substrate. This axisymmetric approximation of the pyramidal Berkovich indenter is commonly used due to the shorter computation times compared to a more accurate three-dimensional pyramidal indenter model. The model of Figure 6 is implemented in ABAQUS standard using large deformation theory and four node bilinear quadrilateral CAX4R elements for both the substrate and the indenter. This axisymmetric model is released as supplementary material in Appendix D, together with ANSYS Workbench implementations, with quadratic elements instead, of the same axisymmetric model as well as a three-dimensional pyramidal indenter model.

The size of the modeled substrate domain is $20\ \mu\text{m} \times 20\ \mu\text{m}$ and the height of the 70.3° half-angle indenter is $8\ \mu\text{m}$. The model delivers self-similar results for indentation depths up to approximately $1/20^{\text{th}}$ of the indenter height [39], i.e. $400\ \text{nm}$ for the chosen model dimensions. For larger indentation depths, boundary effects, especially at the top of the

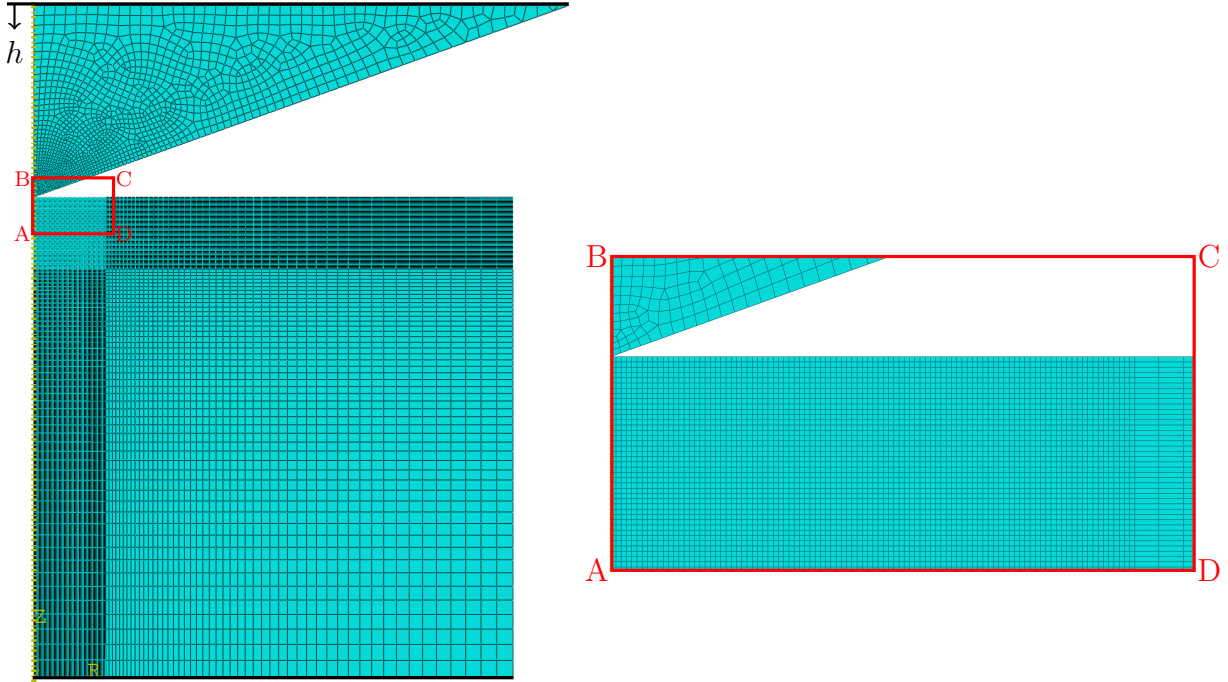


Figure 6: Finite element mesh of the indenter and the substrate and magnification of the contact region.

indenter domain, lead to an artificial size effect. Remark that as clarified in [39], not only the substrate but also the indenter domain needs to be large enough compared to the indentation depth, otherwise misleading conclusions may be reached [40, 41]. As long as the aforesaid indentation depth condition is respected, the obtained results can be considered as self-similar and may therefore be scaled up or down to the desired indentation depth based on the simple scaling law according to Eq. (1). In that sense, the size of the model and the indentation depth are not essential quantities in absolute numbers, but the ratio between the two is important.

In the model, a refined mesh is used near the contact zone, and the size of elements is gradually increased further away from this region. The element size in the contact region is in the order of 0.075 times the indentation depth. All degrees of freedom at the bottom of the substrate domain are constrained, and a symmetry condition is applied along the axis of symmetry. The top of the indenter domain is fixed in the horizontal direction and displaced incrementally in the negative vertical direction. The indentation process is simulated in displacement control mode, with at least 25 increments for the loading phase and at least 100 decrements for the unloading phase. The contact between the substrate and the indenter is assumed to be frictionless. Reference [6] discusses the severity of this assumption.

The indenter domain is modeled with finite strain elasticity, and for the examples shown in the present work, material properties for diamond are considered with Young's modulus $E_i = 1141$ GPa and Poisson's ratio $\nu_i = 0.07$, [42]. Finite-strain elasto-plasticity is used for the substrate domain with Young's modulus E and Poisson's ratio ν . Regarding the plastic response of the substrate, isotropic hardening is assumed, specified through a tabulated

relationship $\sigma(\varepsilon^p)$ between the uniaxial stress σ and the uniaxial plastic strain ε^p . In that sense, any isotropic hardening law can be used, but for the examples shown in the present work, the power-law constitutive equation from [4, 12] is considered

$$\sigma = \begin{cases} E\varepsilon, & \text{for } \sigma \leq \sigma_y \\ \sigma_y \left(\frac{E\varepsilon}{\sigma_y} \right)^n, & \text{for } \sigma \geq \sigma_y \end{cases} \quad (4)$$

where ε is the total strain, σ_y the initial yield limit, and n the hardening exponent. Based on this constitutive law, tabulated ε^p - σ data for the finite element model are generated using the script from Appendix A, consistent with [12] and avoiding the minor approximation done in [4].

This is the usual parametrization of indentation models based on six material parameters E_i , ν_i , E , ν , σ_y , and n . When evaluating depth-sensing indentation experiments, some of these parameters are considered as known, and others are determined by fitting the model against experimental data. The following two examples demonstrate that by fixing E_i , ν_i , ν , and n , the remaining two parameters, E and σ_y , can be determined to reach an excellent fit to the experimental data after blunting distance compensation from Figure 4. Apart from the material properties for the diamond indenter, given above, a Poisson's ratio of $\nu = 0.3$ and a hardening exponent of $n = 0.2$ are assumed for the high strength steel material of Figure 4a while the corresponding values assumed for the fused silica sample of Figure 4b are $\nu = 0.17$ and $n = 0$ [37, 43–45].

The fitting procedure between the finite element model and the experiment can be performed according to [32] but restricted to the two parameters E and σ_y . The optimization loop from [32] can either be implemented programmatically, using for example [46], or it can be performed manually, as is the case in the present work. The outcome of the manual optimization yields the Young's moduli and yield limits provided in Figure 7 for the two example materials. Note that self-similarity of the solution allows to perform all finite element simulations with a fixed maximum indentation displacement, equal to 400 nm in our case. The obtained results can then be converted to the desired maximum indentation depth h_m by scaling lengths and displacements with $h_m/400$, and areas and forces with $(h_m/400)^2$. In that sense, h_m is a free fitting parameter in the optimization.

In fact, h_m can be exploited for simulating the additional deformation during holding time at maximum load, observed experimentally. Although the numerical model cannot physically capture the sinking due to creep and other rate-dependent phenomena, this additional deformation can be simulated through overloading. This is done by allowing h_m to slightly exceed the actual maximum indentation displacement. In this manner, a better approximation of the actual maximum contact area is reached, including the deformation occurred during the holding time.

It should actually not be surprising that an excellent fit is found for both materials shown in Figure 7, despite their hardening exponents n being fixed beforehand. As very clearly demonstrated already in previous works [29, 30], for common structural materials, there is no unique combination of E , σ_y , and n that matches a single indentation force-displacement

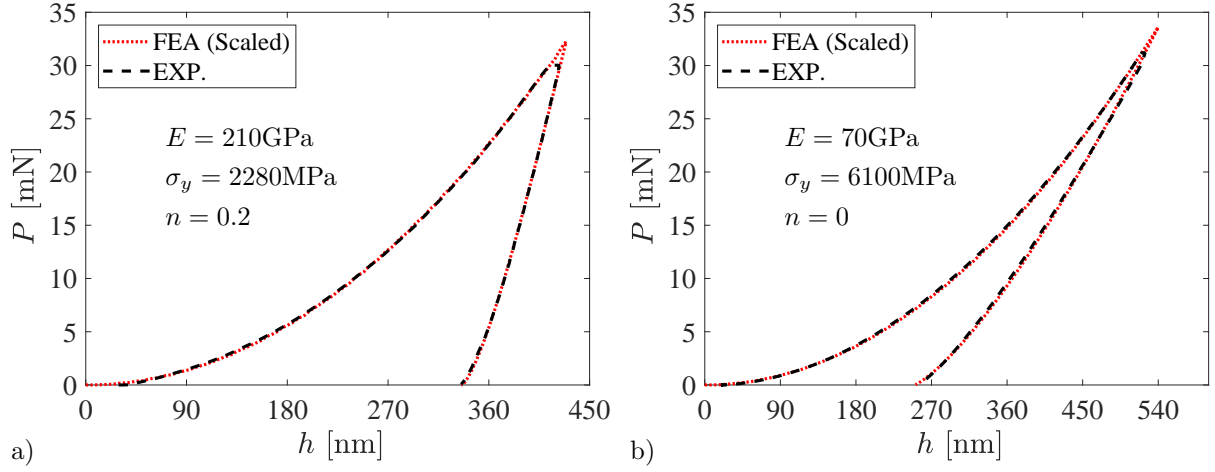


Figure 7: Fitted numerical load-displacement curves against experimental ones by fitting the substrate mechanical properties E and σ_y for the high strength steel (a), assuming a hardening exponent of $n = 0.2$, and for fused silica (b) [38], assuming $n = 0$.

curve. This is also illustrated below, by means of the high strength steel indentation example from Figure 7a, which is now reevaluated for different assumed hardening exponents n . Figure 8 shows that equally good fits against the experimental curve can be reached for $n=0.15$ and $n=0.25$. It is easy to observe that all three solutions ($n=0.15, \sigma_y=2500\text{MPa}$), ($n=0.2, \sigma_y=2280\text{MPa}$), and ($n=0.25, \sigma_y=2060\text{MPa}$) lie on the line $\sigma_y = 3160 - 4400n$ MPa. In general, a prior good knowledge of the material hardening behavior, based e.g. on the literature, is necessary, unless indentation with two distinct indenter angles is performed [7], or measurements of the imprint geometry are taken into account [47, 48]. Figure 8 clearly demonstrates that reverse analyses methods that suggest that three parameters can be determined should be treated with skepticism.

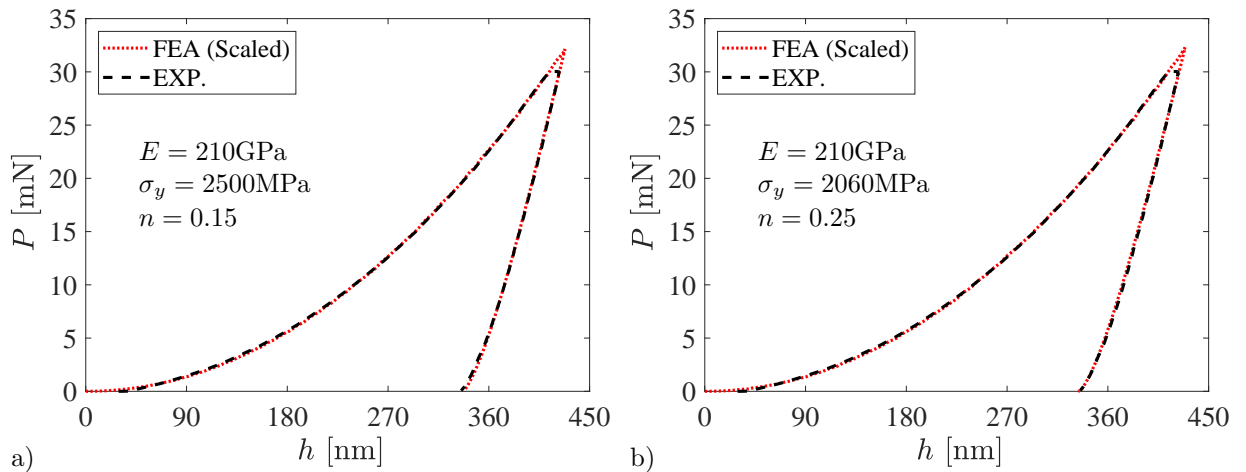


Figure 8: Non-uniqueness of the load-displacement curves with respect to n . Similar quality fittings can be achieved e.g. for $n = 0.15$ (a) and $n = 0.25$ (b).

4. Indenter compliance

By including a sufficiently large portion of the deformable indenter in the finite element model, as explained in Section 3, the effects of indenter compliance are inherently accounted for. It is however useful to quantitatively assess the advantages of this direct approach compared to the commonly used approximation with a rigid indenter. Most of the available reverse analysis methods, such as [4, 12], are actually based on simulations with a rigid indenter. Semi-analytical approaches like [4] assume that virtually identical force-displacements curves will be obtained for different combinations of indenter (E_i, ν_i) and substrate (E, ν) materials as long as they result in the same effective modulus E^* , according to

$$E^* = \left(\frac{1 - \nu^2}{E} + \frac{1 - \nu_i^2}{E_i} \right)^{-1}. \quad (5)$$

Parametric studies in the literature were typically performed with a rigid indenter and a substrate with Poisson's ratio equal to 0.3. The substrate elastic modulus used in such studies will in the following be explicitly denoted as $E_{0.3}$ to avoid any ambiguity, differentiating it from the real substrate elastic modulus E . According to Eq. (5), the relationship

$$E^* = \frac{E_{0.3}}{1 - 0.3^2} \quad \Rightarrow \quad E_{0.3} = 0.91E^* \quad (6)$$

holds between E^* and $E_{0.3}$. Obtained results are reported in the literature either parametrized with regard to E^* , like in [4], or with regard to $E_{0.3}$, like in [12]. It is of utter importance when reading these references to be aware not only of the difference between E^* and E , but also between $E_{0.3}$ and E , as well as to distinguish $E_{0.3}$ from E^* .

In this section, the implications of the rigid indenter approximation compared to the actually modeled compliant indenter will be illustrated by means of a practical example. For this purpose, the case of high strength steel indentation from Figure 7a is reevaluated using two different rigid indenter equivalent models, summarized in Table 1. Substituting the deformable (diamond) indenter with a rigid one requires to reduce the substrate modulus of elasticity from $E = 210$ GPa to $E_{0.3} = 174.8$ GPa in order to maintain the same effective modulus of elasticity $E^* = 192.1$ GPa. This conversion of the original deformable-deformable setting into an equivalent rigid-deformable setting creates also a minor ambiguity which has not been previously discussed in the literature. When calculating the hardening relationship $\sigma(\varepsilon_p)$ based on Eq. (4), one can either use the modulus of the real substrate E or the modulus $E_{0.3}$ of the equivalent substrate material. These two cases are covered in this study and benchmarked against the reference deformable-deformable case.

The parametric study by Dao et al. [4] was based on a rigid indenter and utilized the modulus of elasticity $E_{0.3}$ of the equivalent substrate for deriving the hardening behavior $\sigma(\varepsilon_p)$ according to Eq. (4). To reproduce the same modeling assumptions as in [4], the value $E_{0.3} = 174.8$ GPa is used for the second case in the last column of Table 1. However, to be consistent with the reference deformable-deformable setting, a better approximation is to use the now known actual substrate modulus of elasticity $E = 210$ GPa when extracting the hardening behavior from Eq. (4). This approach defines the last case in Table 1.

Table 1: Cases of deformable and rigid indenter with a common effective modulus $E^* = 192.1$ GPa.

Case	E [GPa]	ν [-]	E_i [GPa]	ν_i [-]	E used in Eq. (4) for extracting $\sigma(\varepsilon_p)$ [GPa]
Deformable	210	0.3	1141	0.07	210
Rigid (Dao et al., 2001)	174.8	0.3	∞	-	174.8
Rigid consistent					210

Figure 9 shows the simulated force-displacement curves obtained for the reference case and the two rigid indenter approximations. Deviations from the reference deformable-deformable case can be observed both regarding the loading and the unloading path. Compared to the reference loading curvature parameter $C = 175.2$ GPa, the corresponding value for the rigid approximation with the same assumptions as by Dao et al. [4] is $C = 171.1$ GPa, i.e. circa 2% lower. Defining the substrate hardening behavior in a more consistent manner leads to $C = 173$ GPa, which is still more than 1% lower than the reference value. Significant deviations are also observed with regard to the unloading paths. As a consequence of these deviations, the ratio between the recovered elastic work and the total indentation work is underestimated by 7%, using the rigid indenter equivalence according to Dao et al. [4], and by 5% with the more consistent definition of the substrate hardening.

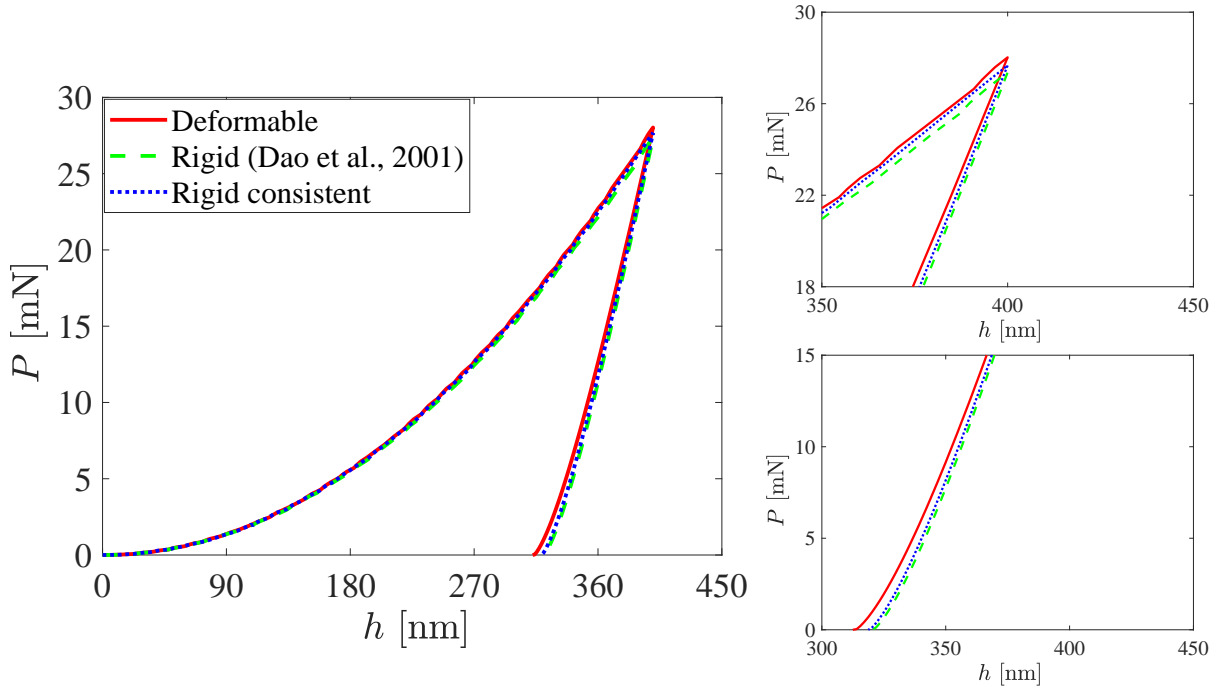


Figure 9: Comparison of force-displacement curves between a reference deformable-deformable indentation setting and two rigid-deformable approximations.

The observed deviations due to the use of the equivalent rigid indenter approximation are by no means negligible for practical applications. As it will be shown in the next section, deviations of a certain magnitude in the loading and unloading path translate into similar relative errors in terms of the material properties predicted by the two-parameter reverse analysis method proposed below. For classical three-parameter reverse analysis methods, the relative errors in terms of the predicted substrate parameters could even be magnified as indicated by the sensitivity analysis provided in [4] for just one representative case.

Actually, even by simply extracting the maximum indenter tip displacement h_{tip} from the compliant indenter model used for the simulations from Figure 7, one can realize that h_{tip} is approximately 5% smaller than the far field displacement h_m imposed on the indenter. Just by this observation, it should be clear that for these relatively stiff and hard substrates, the rigid indenter approximation falls short in accurately describing even simple geometrical magnitudes. Fortunately, the need for improving the available rigid indenter approximations has actually become obsolete after the recent advances in terms of ease of modeling and accessibility to finite element software. All discussed difficulties and ambiguities can easily be avoided altogether by use of a dedicated finite model with the indenter modeled as an elastic body in the first place. Hence, the aim of the present work is not to re-assess how well different semi-analytical models perform in different regions of the entire parameter space, but to propose a practical approach for avoiding all sources of errors and ambiguities that may easily be avoided. In that sense, it is proposed to use semi-analytical models only after re-calibration for a specific material type, as described in the following section, to deal with a narrower range of substrate material parameters resulting in higher accuracy.

5. Hybrid finite element and semi-analytical evaluation

The examples of Section 3 have demonstrated in terms of real indentation measurements that a few iterations of a finite element based forward analysis can lead to a very simple and reliable estimation of E and σ_y for the substrate. This is, in any case, under the condition of having verified measurement self-similarity, having applied blunting distance compensation, and having acknowledged the non-uniqueness with regard to the hardening exponent.

Although such a direct finite element based evaluation is very simple, there are often cases where hundreds of indentation curves need to be evaluated for extracting statistical data. In these cases, semi-analytical methods are still valuable. Nevertheless, they should rather be re-calibrated against a direct finite element based evaluation of one or few representative indentation curves instead of being applied in a black-box manner. Below, we propose a hybrid approach where, in a first phase, a few indentation curves are evaluated by means of a finite element model, and calibration parameters for a semi-analytical method are extracted from these simulations. Then, the calibrated semi-analytical method is applied to the remaining possibly large number of available indentation curves.

5.1. Experimental curve parametrization

After blunting distance compensation, any approximately self-similar indentation force-displacement curve can be described through the loading curvature parameter C and some parametrization of the unloading path, as e.g. illustrated in Figure 10.

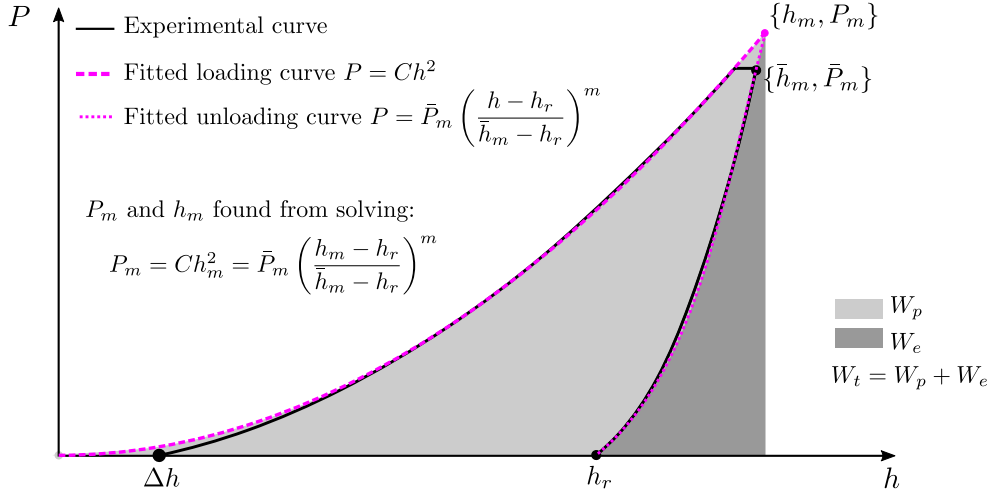


Figure 10: Extracting curve parameters C , h_m , P_m , h_r , and m from an experimental indentation force-displacement curve.

The parameter C is already obtained in the blunting distance compensation procedure as per Section 2, [25]. Regarding the unloading path, the most common parametrization is the power-law fit according to Oliver and Pharr [2], in the form

$$P = \alpha(h - h_r)^m, \quad (7)$$

with the parameters α , h_r , and m describing the unloading path. There are actually many ways of fitting this curve to the experimental data. In most practical cases, the point $\{h_r, 0\}$ at the end of the unloading path can be extracted rather unambiguously. It is also easy to extract a point $\{\bar{h}_m, \bar{P}_m\}$ at the beginning of the unloading path. These two control points can be used to fix α and h_r in Eq. (7), resulting in the expression

$$P = \bar{P}_m \left(\frac{h - h_r}{\bar{h}_m - h_r} \right)^m. \quad (8)$$

Eq. (8) can then be fitted to the experimental data, typically the upper 67% of the unloading path, by least square optimization with respect to the single remaining parameter m .

The next step is to find the intersection point $\{h_m, P_m\}$ between the loading and the unloading paths, according to Figure 10. Although this point is not part of the experimental data, it allows to establish a link between the experiment and any semi-analytical or numerical procedure, based on the assumption that holding time deformation can be reproduced by an overload in the model.

The method presented in the following subsection is rather robust with respect to small changes in the fitting of the unloading path. However, this is not the case for all other methods that rely on the initial slope S of the unloading curve, and an important disclaimer has to be made here. Despite its resemblance to Kick's law Eq. (1), the power-law fit Eq. (7) can by no means reproduce the actual mechanics of the unloading process as they

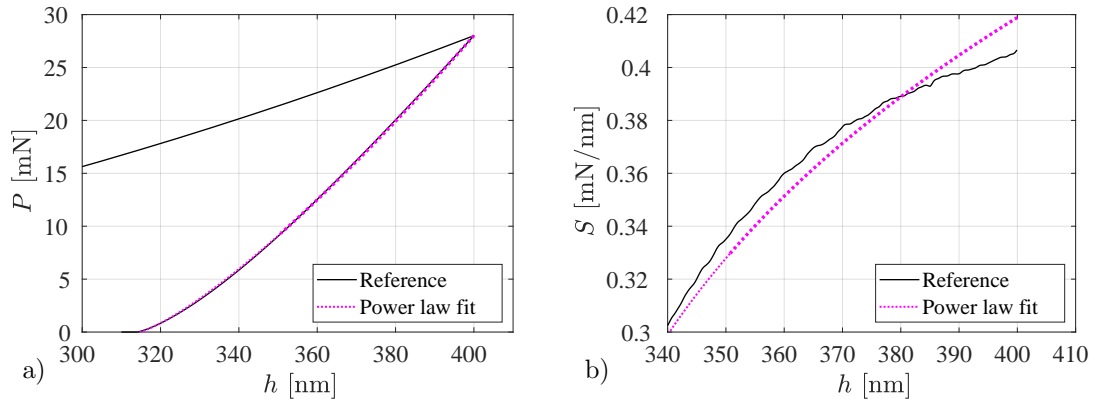


Figure 11: Unloading path power-law fitting against a finite element reference solution (a) and overestimation of the initial unloading slope (b).

are currently understood according to the effective indenter shape interpretation [49, 50]. This is illustrated in Figure 11 where the power-law fit against a reference finite element simulation appears very accurate in a h - P diagram, while it appears very poor when the slope S of the curves is examined. It should be kept in mind that the power-law fit is a phenomenological description without any underlying mechanistic foundation.

5.2. A new semi-analytical reverse analysis method

The motivation for introducing a new reverse analysis method, instead of adapting [4], lies in the practical issues arising from the strong dependence of the estimated initial unloading slope S on the fitting procedure. In combination with the known high sensitivity of three-parameter reverse analysis methods with respect to S [4], it results in the notorious almost mystical impact of the unloading curve fitting procedure on the reverse analysis predictions. What happens in reality is that by slightly changing the fitted interval or other fitting details, analysts have the possibility of greatly affecting the estimated S and thereby implicitly "calibrate" their implementation. In order to avoid this strong sensitivity, a method is proposed in this section that relies on models from the literature that do not involve the initial unloading slope S and Sneddon's formula [51]. The new reverse analysis method is then combined in the following subsection with an explicit and transparent calibration procedure against a case specific finite element model.

The goal is to determine E and σ_y for the substrate, based on C , h_r , h_m , and m extracted from an experimental curve, an assumed Poisson's ratio ν and hardening exponent n for the substrate, and the known indenter properties E_i and ν_i . As a first step, it is easy to calculate the ratio of the recovered elastic work to the total indentation work, cf. Figure 10, as a function of h_r , h_m , and m according to

$$\frac{W_e}{W_t} = \frac{P_m(h_m - h_r)/(m + 1)}{Ch_m^3/3} = \frac{3(1 - h_r/h_m)}{m + 1}. \quad (9)$$

From this point on, the whole unloading path will be characterized by the single dimensionless parameter W_e/W_t .

Based on extensive finite element simulations with rigid indenters, Cheng et al. [8, 52] established the approximate relationship

$$\frac{H}{E^*} = \kappa(\theta) \frac{W_e}{W_t}, \quad (10)$$

where $H = P_m/A_m$ is the hardness under load, A_m the projected contact area at maximum load, and κ a constant that depends only on the semicone angle θ of the indenter.

The same authors proposed the dimensionless functions Π_α and Π_β , which were later approximated in rather simple and accurate form by Ma et al. [12], for the very common case of $\theta = 70.3^\circ$ and $\nu = 0.3$ (reproduced in Appendix B). These more specialized functions from [12] provide basic fitting relationships in the form

$$\frac{P_m}{E_{0.3} h_m^2} = \Pi_\alpha(\sigma_y/E_{0.3}, n) \quad \Rightarrow \quad P_m = E_{0.3} \Pi_\alpha(\sigma_y/E_{0.3}, n) h_m^2 \quad (11)$$

and

$$\frac{h_c}{h_m} = \Pi_\beta(\sigma_y/E_{0.3}, n), \quad (12)$$

where h_c is the height of the portion of the indenter in contact with the substrate under maximum load, called contact depth. The latter equation can be used for estimating the contact area

$$A_m = \pi \tan^2 \theta \Pi_\beta^2(\sigma_y/E_{0.3}, n) h_m^2. \quad (13)$$

Dividing Eq. (11) by Eq. (13) results in a second equation for the hardness H as a function of the unknown ratio $\sigma_y/E_{0.3}$

$$\frac{H}{E_{0.3}} = \frac{\Pi_\alpha(\sigma_y/E_{0.3}, n)}{\pi \tan^2 \theta \Pi_\beta^2(\sigma_y/E_{0.3}, n)}, \quad (14)$$

Combining Eqs. (10) and (14) while accounting for Eq. (6) results in an equation that can be solved for the ratio $\sigma_y/E_{0.3}$

$$\Pi_\alpha(\sigma_y/E_{0.3}, n) - c_\kappa \frac{W_e}{W_t} \Pi_\beta^2(\sigma_y/E_{0.3}, n) = 0 \quad (15)$$

with

$$c_\kappa = \frac{\kappa(\theta) \pi \tan^2 \theta}{0.91}, \quad \theta = 70.3^\circ. \quad (16)$$

The restriction to $\theta = 70.3^\circ$ is due to the use of Π_α and Π_β from [12], but otherwise the method could be applied independent of the indenter semicone angle.

After solving Eq. (15) for $\sigma_y/E_{0.3}$, the Π_α function can be used to compute $E_{0.3}$ as

$$E_{0.3} = C / \Pi_\alpha(\sigma_y/E_{0.3}, n), \quad (17)$$

and finally E can be computed through Eqs. (6) and (5), and σ_y is computed from the now known ratio $\sigma_y/E_{0.3}$.

5.3. Calibration of the semi-analytical method

Although Eq. (10) and the dimensionless functions Π_α and Π_β can approximate the indentation process for a wide range of substrate material parameters, there will always be inaccuracies. These are inevitable due to the nature of the fitting procedure but also due to modeling simplifications like the indenter compliance effects discussed in Section 4. Given the current availability of finite element models for conical indentation, there is no reason for accepting these inaccuracies. Instead, a finite element simulation according to Section 3 can be used as a reference for re-calibrating the semi-analytical functions. The simulation used for this re-calibration needs to be manually fitted to one representative measurement among the series of indentations that need to be evaluated in total.

To obtain a complete overview of the case being evaluated and avoid possible mistakes and ambiguities, one should start with an inventory of all geometrical and physical quantities involved in the fitted finite element analysis. Table 2 demonstrates this kind of inventory for the two simulations included in Figure 7. Essential quantities in this inventory are the reference values for C and W_e/W_t , extracted from the simulated force-displacement curve. Moreover, the contact radius r_c is determined by locating the last contact point between the indenter and the substrate in the finite element model at maximum load. The contact radius is directly linked to the projected contact area through $A_m = \pi r_c^2$. If a three-dimensional pyramidal indenter model is used instead of an axisymmetric one, then A_m needs to be directly estimated in the finite element model instead of r_c . These essential parameters from Table 2 allow to calculate the calibration factors

$$s_\alpha = \frac{C}{E_{0.3}} \frac{1}{\Pi_\alpha(\sigma_y/E_{0.3}, n)}, \quad s_\beta = \frac{r_c}{\tan(\theta) h_m} \frac{1}{\Pi_\beta(\sigma_y/E_{0.3}, n)} \quad (18)$$

and

$$\bar{c}_\kappa = \frac{C}{E_{0.3}} \left(\frac{r_c}{\tan(\theta) h_m} \right)^{-2} \left(\frac{W_e}{W_t} \right)^{-1}. \quad (19)$$

Then, one can simply substitute Π_α and Π_β in Eqs. (11)-(17) with the calibrated functions $\bar{\Pi}_\alpha = s_\alpha \Pi_\alpha$ and $\bar{\Pi}_\beta = s_\beta \Pi_\beta$, respectively, and c_κ in Eq. (15) with \bar{c}_κ .

This re-calibration of the original fitted equations allows for a greater accuracy within a narrower range of material parameters for the specific material of interest. It mitigates discrepancies due to the fitting procedure and modeling assumptions of the original works, and it opens up for the possibility of accounting for additional effects. If for example, a three-dimensional finite element model with a pyramidal indenter is used for the calibration, inaccuracies due to the conical indenter simplification can be eliminated as well.

Applying this procedure with the data from Table 2 results in $s_\alpha = 0.989$, $s_\beta = 0.973$, and $\bar{c}_\kappa = 4.492$ for the hardened steel case and $s_\alpha = 0.949$, $s_\beta = 0.994$, and $\bar{c}_\kappa = 5.414$ for the case of fused silica. It should be noted that using the $\kappa(\theta)$ function from [52] (reproduced in Appendix B), for $\theta = 70.3^\circ$, results in $c_\kappa = 4.695$. The observed deviations of s_α and s_β from unity as well as of \bar{c}_κ from c_κ express all combined inaccuracies in the respective semi-analytical equations, compared to the more accurate finite element simulations of the present work.

Table 2: Inventory of geometrical, physical, and mathematical quantities involved in the evaluation of two representative finite element simulations. The table sections correspond to: input material data, imposed indenter displacement, geometrical data from the deformed model at maximum load, and data extracted from the obtained force-displacement curve.

	hardened steel		fused silica		
	numer. scale	phys. scale	numer. scale	phys. scale	
Substrate modulus of elasticity E	210		70		GPa
Substrate Poisson's ratio ν	0.3		0.17		-
Substrate yield limit σ_y	2280		6100		MPa
Substrate hardening exponent n	0.2		0		-
Max. indentation displacement h_m	400	429	400	540	nm
Max. indenter tip displacement h_{tip}	381.1	408.8	381.5	515.1	nm
Max. contact radius r_c	990.0	1062	788.5	1064	nm
Max. projected contact area $A_m = \pi r_c^2$	3.079	3.542	1.953	3.560	μm^2
Max. contact force P_m	28.03	32.24	18.43	33.60	mN
Loading curvature parameter $C = P_m/h_m^2$		175.2		115.2	GPa
Residual indenter tip displacement h_r	313.8	336.5	185.3	250.2	nm
Recovered work ratio W_e/W_t		0.284		0.692	-
Loaded hardness $H = P_m/A_m$		9102		9438	MPa

Finally, the aforesaid calibrations for the two material types were used for performing a reverse analysis of the experimental curves from Figure 7, according to subsection 5.2. The calibrated reverse analysis for the hardened steel nanoindentation measurement resulted in $E = 214$ GPa and $\sigma_y = 2221$ MPa while the material parameters $E = 69.3$ GPa and $\sigma_y = 6252$ MPa were obtained for fused silica. The deviations observed between the values obtained and the corresponding material parameters from the fitted finite element simulations correspond to a realistic level of expectations regarding the precision for this type of evaluations. The predicted loaded hardness values according to Eq. (14) are 8973 MPa for the hardened steel and 9477 MPa for the fused silica sample, which are fairly close to the corresponding values in Table 2.

In order to promote transparency and avoid any possible ambiguities, the Matlab/Octave code implementing the theory of Section 2 and subsections 5.2 and 5.3, used for producing the presented results, is made available in Appendix C.

5.4. Sensitivity analysis

In order to give an indication of the robustness of the method proposed in this section, sensitivity analysis results are provided in Table 3, for two representative cases. For these specific examples, it is shown that relative errors in the C and W_e/W_t parameters, extracted from experimental data, result in similar relative errors in terms of the estimated material parameters E and σ_y . Hence, this two-parameter reverse analysis method induces no considerable error magnification. Three-parameter reverse analysis methods typically have much

larger sensitivities [4], which is simply a manifestation of the underlying lack of uniqueness, discussed in connection to Figure 8.

Table 3: Sensitivity of the two-parameter (E and σ_y) reverse analysis method with regard to the input parameters C and W_e/W_t , for two representative cases.

Hardened steel ($\sigma_y/E \approx 0.011$, $n=0.2$)				Fused silica ($\sigma_y/E \approx 0.087$, $n=0$)			
		$C[\pm 1\%]$	$W_e/W_t[\pm 1\%]$			$C[\pm 1\%]$	$W_e/W_t[\pm 1\%]$
Output	E	$\pm 1.2\%$	$\mp 0.8\%$	Output	E	$\pm 1.1\%$	$\mp 0.8\%$
	σ_y	$\pm 1\%$	$\pm 0.7\%$		σ_y	$\pm 1\%$	$\pm 1.7\%$

6. Conclusions

With the help of illustrative practical examples, this work aimed at rationalizing the evaluation of depth-sensing indentation experiments and reassessing and revisiting established practices in the view of the current availability of simulation tools. A central element in the proposed pragmatic approach is the identification of self-similarity in an experimental measurement and subsequent blunting distance compensation. Blunting distance compensation is a procedure known since the 90s but to the best knowledge of the authors never endorsed by equipment manufacturers or standardization entities. In the present work, it was illustrated how blunting distance compensation is actually essential for presenting experimental results in a universal and laboratory independent manner. At the same time, it makes the experimental data compatible with methods that rely on sharp indentation simulations.

Based on a sharp indentation finite element model, assuming a hardening exponent and sweeping a range of Young's moduli and yield strengths for the substrate, a very good match between simulation and an experiment can easily be obtained. This was demonstrated for fused silica and high strength steel substrates. In order to facilitate the adoption of this direct simulation approach, finite element models are made available for conical and pyramidal indentation with a deformable indenter, for two major commercial finite element packages (ABAQUS & ANSYS). Essential modeling aspects in the released models were also documented and discussed. Although all examples in this paper were limited to the geometrically simplified case of conical indentation, the general approach is directly applicable to pyramidal indentation simply by employing a corresponding three-dimensional finite element model as the one from Appendix D.

The advantages of direct simulations compared to semi-analytical models were discussed in detail by exemplifying common sources of inaccuracies in the latter. Special attention was given to the inaccuracies introduced by the equivalent rigid indenter approximation. Finally, this work proposed a new semi-analytical reverse analysis method, based on available fitted functions from the literature, which does not rely on the initial unloading slope S and Sneddon's equation. To mitigate the inevitable inaccuracies when working with semi-analytical and fitted equations, a calibration procedure was proposed, which allows the application of the semi-analytical method in a narrower range of substrate material parameters around the calibration point.

One important aspect discussed within the present critical review is the lack of uniqueness in three-parameter reverse analysis methods. Without repeating a comprehensive investigation of the entire parametric space, already available in the literature, the present work demonstrated this issue by a simple practical example. The implications of this inherent limitation of depth-sensing indentation were discussed, especially with regard to the need for an independent estimation of the substrate hardening exponent n . Using additional information from a second indentation with a different indenter angle or using measurements of the indentation imprint geometry are possible solutions to this limitation.

Acknowledgement

This work is supported by the Innovation Fund Denmark through the WhiteWind project (Grant 7046-00003B). The authors would like to thank Dr. Matteo Villa and Dr. Ömer Can Kücüküydiz for their help with nanoindentation measurements, and Dr. Sebastian Bruns for providing fused silica indentation data.

Data Availability Statement

The datasets generated and supporting the findings of this article are obtainable from the corresponding author upon reasonable request. See Appendix D for the released models.

Appendices

A. Generation of tabulated ε^p - σ data

For given Young's modulus E , yield limit σ_y , and hardening exponent n , tabulated data for a $\sigma(\varepsilon^p)$ relationship are generated according to [12], using the following Matlab/Octave function.

```
function print_powerlaw_data(E, sy, n) % E, sy in MPa
    ep = [0:0.00025:0.001,0.002:0.002:0.1,0.12:0.02:2]';
    for m = 1:length(ep)
        f = @(s) s-(sy*((s/sy)+(E/sy)*ep(m))^n);
        fprintf('%f %f\n', ep(m), fsolve(f,sy,optimset('Display','off')));
    end
end
```

B. Dimensionless functions Π_α , Π_β , and $\kappa(\theta)$

The Π_α and Π_β functions according to [12] are:

$$\Pi_\alpha(\bar{\sigma}_y, n) = (2.77 - 2.11n) \bar{\sigma}_y^{-0.064 \ln(\bar{\sigma}_y) - 0.42n} \quad (\text{B1})$$

$$\Pi_\beta(\bar{\sigma}_y, n) = 0.7 + 0.55 e^{-2.16n - 40.32(\bar{\sigma}_y)} \quad (\text{B2})$$

where $\bar{\sigma}_y = \sigma_y/E_{0.3}$.

The $\kappa(\theta)$ function according to [8, 52] is:

$$\kappa(\theta) = 1/[1.27(1.5 \tan(\theta) + 0.327)], \quad (\text{B3})$$

where $\theta = 70.3^\circ$ for a Berkovich indenter.

C. Code for calibration and use of the semi-analytical model

```

function evaluate_indentation(h, P, experim, nu, n, E_i, nu_i)
% h in nm, P in mN
% nu, n: assumed substrate parameters
% E_i in MPa, nu_i: indenter parameters
if exist('OCTAVE_VERSION', 'builtin') ~= 0
    pkg load optim
end

% Ma's PIalpha function x = sigmay/E03
PIalpha = @(x,n) (2.77 - 2.11*n) * x.^(-0.064*log(x) - 0.42*n);
% Ma's PIBeta function x = sigmay/E03
PIbeta = @(x,n) 0.7 + 0.55*exp(-2.16*n - 40.32*x);
c_kappa0 = (pi*tan(70.3*pi/180)^2)/(1-0.3^2)/(1.27*(1.5*tan(70.3*pi/180)+0.327));

% Calibration data
clb_case = 1; % 1: hardened steel, 2: fused silica
%Input to FEA:
E_clb = getfield([ 210e3, 70e3], {clb_case}); % MPa
nu_clb = getfield([ 0.3, 0.17], {clb_case});
sigmay_clb = getfield([ 2280, 6100], {clb_case}); % MPa
n_clb = getfield([ 0.2, 0], {clb_case});
hm_clb = getfield([ 400., 400.], {clb_case}); % nm
%Auxiliary quantities
E03_clb = (1-0.3^2)/((1-nu_clb^2)/E_clb + (1-nu_i^2)/E_i);
%Output from FEA
Pm_clb = getfield([28.027,18.434], {clb_case}); % mN
C_clb = 1e9*Pm_clb/hm_clb^2; % MPa
Wratio_clb = getfield([0.284039,0.692151], {clb_case});
Am_clb = getfield([3.0794e6,1.9532e6], {clb_case}); % nm^2
hc_clb = sqrt(Am_clb/pi)/tan(70.3*pi/180);

% calibration multiplier for Ma's PIalpha function
s_alpha = C_clb/E03_clb / PIalpha(sigmay_clb/E03_clb,n_clb);
% calibration multiplier for Ma's PIBeta function
s_beta = hc_clb/hm_clb / PIbeta(sigmay_clb/E03_clb,n_clb);
% calibrated factor for work ratio function
c_kappa = C_clb/E03_clb / ((hc_clb/hm_clb)^2*Wratio_clb);
fprintf('s_alpha=%f\ns_beta=%f\nc_kappa=%f\n', s_alpha, s_beta, c_kappa);

maxpos = find(P>0.999*max(P), 1, 'first');
if experim
    params = polyfit(h(P(1:maxpos) > 0.1*P(maxpos)), ...
                    sqrt(P(P(1:maxpos) > 0.1*P(maxpos))), 1);
    C = 1e9*params(:,1)^2;
    Dh = params(:,2)/params(:,1);
    h = h + Dh;

    maxpos = find(P>0.98*max(P), 1, 'last');
    minpos = find(P>1e-5*max(P), 1, 'last');
    h_unloading = h(maxpos:minpos);
    P_unloading = P(maxpos:minpos);
    hr = polyfit(P_unloading(end-1:end),h_unloading(end-1:end),1)*[0;1];
    hm_ = h_unloading(1);
    Pm_ = P_unloading(1);
    sel = P_unloading > 0.33*Pm_;
    m = lsqlin(log((h_unloading(sel)-hr)/(hm_-hr)),log(P_unloading(sel)/Pm_), [], []);
    a = Pm_/(hm_-hr)^m;
    % Compensate for holding time deformation
    f = @(h) 1e-9*C*h^2 - a*(h-hr)^m;
    hm = fsolve(f, hm_); % corrected hm_ for holding time deformation
    Pm = 1e-9*C*hm^2; % corrected Pm_ for holding time deformation
else
    minpos = find(P>1e-5*max(P), 1, 'last');
    h_unloading = h(maxpos:minpos);
    P_unloading = P(maxpos:minpos);
    hr = polyfit(P_unloading(end-1:end),h_unloading(end-1:end),1)*[0;1];
    hm = h_unloading(1);
    Pm = P_unloading(1);
    C = 1e9*Pm/hm^2; % MPa
    sel = P_unloading > 0.33*Pm;

```

```

    m = lsqlin(log((h_unloading(sel)-hr)/(hm-hr)),log(P_unloading(sel)/Pm),[],[]);
    a = Pm/(hm-hr)^m;
end

h_fit = hr+(0:0.01:1)*(hm-hr);
figure(1); clf
plot(h, P, 'r'); hold on
plot(h_fit, a*(h_fit-hr).^m, '--b')

Wt = 1e-12*C*hm^3/3; % nJ
We = 1e-3*a/(m+1)*(hm-hr)^(m+1); % nJ
fprintf('We/Wt=%f\n', We/Wt);

% find sigmay/E03 ratio
f = @(x) s_alpha*PIalpha(x,n) - c_kappa*(s_beta*PIbeta(x,n))^2*We/Wt;
sigmay_over_E03 = fsolve(f, sigmay_clb/E03_clb);
% find max contact area
Am = pi*(tan(70.3*pi/180) * hm * s_beta*PIbeta(sigmay_over_E03, n))^2;
% find E
E03 = C/(s_alpha*PIalpha(sigmay_over_E03, n));
E = (1- nu^2) / ((1-0.3^2)/E03-(1-nu_i^2)/E_i);
% find sigmay
sigmay = sigmay_over_E03 * E03;
fprintf('sigmay/E03=%f\nAm=%f\nE=%f GPa\nsigmay=%f MPa\nH=%f MPa\n',...
        sigmay_over_E03, Am, E/1000, sigmay, 1e9*Pm/Am);

end

```

D. Released finite element models

ABAQUS and ANSYS implementations of the sharp indentation finite element model of the present work can be downloaded at <http://dx.doi.org/10.17632/w9bfvb3yft.1>

References

- [1] J. B. Pethica, R. Hutchings, and W. C. Oliver. Hardness measurement at penetration depths as small as 20 nm. *Philosophical Magazine A: Physics of Condensed Matter, Defects and Mechanical Properties*, 48(4):593–606, 1983. ISSN 14606992, 01418610.
- [2] W. Oliver and G. Pharr. An improved technique for determining hardness and elastic modulus using load and displacement sensing indentation experiments. *Journal of Materials Research*, 7(6):1564–1583, 1992. ISSN 20445326, 08842914. doi: 10.1557/JMR.1992.1564.
- [3] W. Oliver and G. Pharr. Measurement of hardness and elastic modulus by instrumented indentation: Advances in understanding and refinements to methodology. *Journal of Materials Research*, 19(1):3–20, 2004. ISSN 20445326, 08842914. doi: 10.1557/jmr.2004.19.1.3.
- [4] M. Dao, N. Chollacoop, K. J. Van Vliet, T. A. Venkatesh, and S. Suresh. Computational modeling of the forward and reverse problems in instrumented sharp indentation. *Acta Materialia*, 49(19):3899–3918, 2001. ISSN 18732453, 13596454. doi: 10.1016/S1359-6454(01)00295-6.
- [5] Y. T. Cheng and C. M. Cheng. Scaling approach to conical indentation in elastic-plastic solids with work hardening. *Journal of Applied Physics*, 84(3):1284–1291, 1998. ISSN 10897550, 00218979. doi: 10.1063/1.368196.
- [6] J. L. Bucaille, S. Stauss, E. Felder, and J. Michler. Determination of plastic properties of metals by instrumented indentation using different sharp indenters. *Acta Materialia*, 51(6):1663–1678, 2003. ISSN 18732453, 13596454. doi: 10.1016/S1359-6454(02)00568-2.
- [7] N. Chollacoop, M. Dao, and S. Suresh. Depth-sensing instrumented indentation with dual sharp indenters. *Acta Materialia*, 51(13):3713–3729, 2003. ISSN 18732453, 13596454. doi: 10.1016/S1359-6454(03)00186-1.
- [8] Y. T. Cheng and C. M. Cheng. Scaling, dimensional analysis, and indentation measurements. *Materials Science and Engineering R: Reports*, 44(4-5):91–149, 2004. ISSN 1879212x, 0927796x. doi: 10.1016/j.mser.2004.05.001.

- [9] N. Ogasawara, N. Chiba, and X. Chen. Measuring the plastic properties of bulk materials by single indentation test. *Scripta Materialia*, 54(1):65–70, 2006. ISSN 18728456, 13596462. doi: 10.1016/j.scriptamat.2005.09.009.
- [10] J. Luo and J. Lin. A study on the determination of plastic properties of metals by instrumented indentation using two sharp indenters. *International Journal of Solids and Structures*, 44(18-19):5803–5817, 2007. ISSN 18792146, 00207683. doi: 10.1016/j.ijsolstr.2007.01.029.
- [11] J. Yan, A. M. Karlsson, and X. Chen. Determining plastic properties of a material with residual stress by using conical indentation. *International Journal of Solids and Structures*, 44(11-12):3720–3737, 2007. ISSN 18792146, 00207683. doi: 10.1016/j.ijsolstr.2006.10.017.
- [12] Z. S. Ma, Y. C. Zhou, S. G. Long, and C. S. Lu. An inverse approach for extracting elastic-plastic properties of thin films from small scale sharp indentation. *Journal of Materials Science and Technology*, 28(7):626–635, 2012. ISSN 19411162, 10050302. doi: 10.1016/S1005-0302(12)60108-X.
- [13] T. H. Pham, J. J. Kim, and S. E. Kim. Estimating constitutive equation of structural steel using indentation. *International Journal of Mechanical Sciences*, 90:151–161, 2015. ISSN 18792162, 00207403. doi: 10.1016/j.ijmecsci.2014.11.007, 10.1016/j.ijmecsci.2014.11.007.
- [14] N. Zhao, Y. Zhao, J. Li, H. Liu, T. Shao, Y. Xu, X. Wang, Z. Lu, J. Chen, X. Liu, and S. Niu. Hardness and yield strength of micro-nano TaC-Fe composite layer characterized through nano-indentation, finite element simulation and dimensional analysis. *Ceramics International*, 46(3):3479–3489, 2020. ISSN 18733956, 02728842. doi: 10.1016/j.ceramint.2019.10.062.
- [15] W. W. Gerberich, J. C. Nelson, E. T. Lilleodden, P. Anderson, and J. T. Wroblek. Indentation induced dislocation nucleation: The initial yield point. *Acta Materialia*, 44(9):3585–3598, 1996. ISSN 18732453, 13596454. doi: 10.1016/1359-6454(96)00010-9.
- [16] N. Fleck and J. Hutchinson. A phenomenological theory for strain gradient effects in plasticity. *Journal of the Mechanics and Physics of Solids*, 41(12):1825–1857, 1993. ISSN 18734782, 00225096.
- [17] H. Gao, Y. Huang, W. D. Nix, and J. W. Hutchinson. Mechanism-based strain gradient plasticity - I. theory. *Journal of the Mechanics and Physics of Solids*, 47(6):1239–1263, 1999. ISSN 18734782, 00225096. doi: 10.1016/S0022-5096(98)00103-3.
- [18] Y. Murakami, K. Tanaka, M. Itokazu, and A. Shimamoto. Elastic analysis of triangular pyramidal indentation by the finite-element method and its application to nano-indentation measurement of glasses. *Philosophical Magazine A-physics of Condensed Matter Structure Defects and Mechanical Properties*, 69(6):1131–1153, 1994. ISSN 14606992, 01418610. doi: 10.1080/01418619408242244.
- [19] Y. T. Cheng and C. M. Cheng. Further analysis of indentation loading curves: Effects of tip rounding on mechanical property measurements. *Journal of Materials Research*, 13(4):1059–1064, 1998. ISSN 20445326, 08842914.
- [20] M. Troyon and M. Martin. A critical examination of the $P-h^2$ relationship in nanoindentation. *Applied Physics Letters*, 83(5):863–865, 2003. ISSN 10773118, 00036951. doi: 10.1063/1.1596384.
- [21] M. Troyon and L. Huang. Correction factor for contact area in nanoindentation measurements. *Journal of Materials Research*, 20(3):610–617, 2005. ISSN 20445326, 08842914. doi: 10.1557/JMR.2005.0099.
- [22] I. Choi, O. Kraft, and R. Schwaiger. Validity of the reduced modulus concept to describe indentation loading response for elastoplastic materials with sharp indenters. *Journal of Materials Research*, 24(3):998–1006, 2009. ISSN 20445326, 08842914. doi: 10.1557/jmr.2009.0120.
- [23] M. Troyon, F. Abbes, and J. A. Garcia Guzman. Is the exponent $3/2$ justified in analysis of loading curve of pyramidal nanoindentations? *Scanning*, 34(6):410–417, 2012. ISSN 19328745, 01610457. doi: 10.1002/sca.21025.
- [24] J. Krier, J. Breuils, L. Jacomine, and H. Pelletier. Introduction of the real tip defect of Berkovich indenter to reproduce with FEM nanoindentation test at shallow penetration depth. *Journal of Materials Research*, 27(1):28–38, 2012. ISSN 20445326, 08842914. doi: 10.1557/jmr.2011.387.
- [25] V. Keryvin, L. Charleux, C. Bernard, and M. Nivard. The influence of indenter tip imperfection and deformability on analysing instrumented indentation tests at shallow depths of penetration on stiff and hard materials. *Experimental Mechanics*, 57(7):1107–1113, 2017. ISSN 17412765, 00144851. doi: 10.1007/s11340-017-0267-1.

- [26] S. V. Hainsworth, H. W. Chandler, and T. F. Page. Analysis of nanoindentation load-displacement loading curves. *Journal of Materials Research*, 11(8):1987–1995, 1996. ISSN 20445326, 08842914. doi: 10.1557/JMR.1996.0250.
- [27] A. C. Fischer-Cripps. Use of combined elastic modulus in depth-sensing indentation with a conical indenter. *Journal of Materials Research*, 18(5):1043–1045, 2003. ISSN 20445326, 08842914. doi: 10.1557/JMR.2003.0144.
- [28] S. A. Rodríguez, J. Alcalá, and R. M. Souza. The reduced modulus in the analysis of sharp instrumented indentation tests. *Journal of Materials Research*, 27(16):2148–2160, 2012. ISSN 20445326, 08842914. doi: 10.1557/jmr.2012.164.
- [29] X. Chen, N. Ogasawara, M. Zhao, and N. Chiba. On the uniqueness of measuring elastoplastic properties from indentation: The indistinguishable mystical materials. *Journal of the Mechanics and Physics of Solids*, 55(8):1618–1660, 2007. ISSN 18734782, 00225096. doi: 10.1016/j.jmps.2007.01.010.
- [30] Y. T. Cheng and C. M. Cheng. Can stress-strain relationships be obtained from indentation curves using conical and pyramidal indenters? *Journal of Materials Research*, 14(9):3493–3496, 1999. ISSN 20445326, 08842914. doi: 10.1557/JMR.1999.0472.
- [31] J. K. Phadikar, T. A. Bogetti, and A. M. Karlsson. On the uniqueness and sensitivity of indentation testing of isotropic materials. *International Journal of Solids and Structures*, 50(20-21):3242–3253, 2013. ISSN 18792146, 00207683. doi: 10.1016/j.ijsolstr.2013.05.028.
- [32] J. J. Kang, A. A. Becker, and W. Sun. Determining elastic-plastic properties from indentation data obtained from finite element simulations and experimental results. *International Journal of Mechanical Sciences*, 62(1):34–46, 2012. ISSN 18792162, 00207403. doi: 10.1016/j.ijmecsci.2012.05.011.
- [33] F. Yuan, P. Jiang, J. Xie, and X. Wu. Analysis of spherical indentation of materials with plastically graded surface layer. *International Journal of Solids and Structures*, 49(3):527–536, 2012. ISSN 0020-7683. doi: 10.1016/j.ijsolstr.2011.10.018.
- [34] G. Bolzon, G. Maier, and M. Panico. Material model calibration by indentation, imprint mapping and inverse analysis. *International Journal of Solids and Structures*, 41(11):2957–2975, 2004. ISSN 0020-7683. doi: 10.1016/j.ijsolstr.2004.01.025.
- [35] O. Iracheta, C. J. Bennett, and W. Sun. A holistic inverse approach based on a multi-objective function optimisation model to recover elastic-plastic properties of materials from the depth-sensing indentation test. *Journal of the Mechanics and Physics of Solids*, 128:1–20, 2019. ISSN 18734782, 00225096. doi: 10.1016/j.jmps.2019.04.001.
- [36] J. L. Loubet, J. M. Georges, and G. Meille. Vickers indentation curves of elastoplastic materials. In P. J. Blau and B. R. Lawn, editors, *Microindentation Techniques in Materials Science and Engineering*, pages 72–89. ASTM International, West Conshohocken, PA, 1985.
- [37] C. Gao and M. Liu. Instrumented indentation of fused silica by Berkovich indenter. *Journal of Non-crystalline Solids*, 475:151–160, 2017. ISSN 18734812, 00223093. doi: 10.1016/j.jnoncrysol.2017.09.006.
- [38] S. Bruns, T. Uesbeck, S. Fuhrmann, M. Tarragó Aymerich, L. Wondraczek, de D. Ligny, and K. Durst. Indentation densification of fused silica assessed by raman spectroscopy and constitutive finite element analysis. *Journal of the American Ceramic Society*, 103(5):3076–3088, 2020. doi: 10.1111/jace.17024.
- [39] Y. P. Cao, M. Dao, and J. Lu. A precise correcting method for the study of the superhard material using nanoindentation tests. *Journal of Materials Research*, 22(5):1255–1264, 2007. ISSN 20445326, 08842914. doi: 10.1557/jmr.2007.0150.
- [40] M. M. Chaudhri. A note on a common mistake in the analysis of nanoindentation data. *Journal of Materials Research*, 16(2):336–339, 2001. ISSN 20445326, 08842914.
- [41] Y. Y. Lim and M. M. Chaudhri. Experimental investigations of the normal loading of elastic spherical and conical indenters on to elastic flats. *Philosophical Magazine*, 83(30):3427–3462, 2003. ISSN 14786435, 14786443.
- [42] G. Simmons and H. Wang. *Single crystal elastic constants and calculated aggregate properties: A handbook*. MIT Press, Cambridge, MA, 1971. ISBN 0262190923.
- [43] Z. Gan, Y. Zhang, G. Yu, C. M. Tan, S. P. Lau, and B. K. Tay. Intrinsic mechanical properties of diamond-like carbon thin films deposited by filtered cathodic vacuum arc. *Journal of Applied Physics*,

- 95(7):3509–3515, 2004. ISSN 10897550, 00218979. doi: 10.1063/1.1667005.
- [44] Z. H. Xu and X. Li. Effect of sample tilt on nanoindentation behaviour of materials. *Philosophical Magazine*, 87(16):2299–2312, 2007. ISSN 14786443, 14786435. doi: 10.1080/14786430601175516.
- [45] R. Hill. *The mathematical theory of plasticity*. The Clarendon Press, Oxford, NY, 1950.
- [46] G. Papazafeiropoulos, M. Muñoz-Calvente, and E. Martínez Pañeda. Abaqus2matlab: A suitable tool for finite element post-processing. *Advances in Engineering Software*, 105:9–16, 2017. ISSN 18735339, 09659978. doi: 10.1016/j.advengsoft.2017.01.006.
- [47] M. Wang, J. Wu, Y. Hui, Z. Zhang, X. Zhan, and R. Guo. Identification of elastic-plastic properties of metal materials by using the residual imprint of spherical indentation. *Materials Science and Engineering a*, 679:143–154, 2017. ISSN 18734936, 09215093. doi: 10.1016/j.msea.2016.10.025.
- [48] Y. Zhang, J. D. Hart, and A. Needleman. Identification of plastic properties from conical indentation using a Bayesian-type statistical approach. *Journal of Applied Mechanics, Transactions ASME*, 86(1):011002, 2019. ISSN 15289036, 00218936. doi: 10.1115/1.4041352.
- [49] G. M. Pharr and A. Bolshakov. Understanding nanoindentation unloading curves. *Journal of Materials Research*, 17(10):2660–2671, 2002. doi: 10.1557/JMR.2002.0386.
- [50] T. Andriollo, J. Thorborg, and J. H. Hattel. Analysis of the equivalent indenter concept used to extract Young’s modulus from a nano-indentation test: some new insights into the Oliver–Pharr method. *Modelling and Simulation in Materials Science and Engineering*, 25(4):045004, 2017. ISSN 1361651x, 09650393. doi: 10.1088/1361-651X/aa6831.
- [51] I. N. Sneddon. The relation between load and penetration in the axisymmetric Boussinesq problem for a punch of arbitrary profile. *International Journal of Engineering Science*, 3(1):47–57, 1965. ISSN 00207225.
- [52] Y. T. Cheng, Z. Li, and C. M. Cheng. Scaling relationships for indentation measurements. *Philosophical Magazine A: Physics of Condensed Matter, Structure, Defects and Mechanical Properties*, 82(10):1821–1829, 2002. ISSN 14606992, 01418610. doi: 10.1080/01418610208235693.